

Mechanical properties of CVD synthesised polycrystalline diamond

In this paper, by R. Ikeda, H. Ogi, T. Ogawa and M. Takemoto, the mechanical properties (elastic stiffness and fracture strength) were measured of polycrystalline diamond film with different structure synthesised by chemical vapour deposition method. Advanced new methods for the evaluation were utilised. Elastic stiffness (C_{11} , C_{12} , C_{14}) was measured by resonant-ultrasound spectroscopy. The stiffness changed by grain boundary (GB) structure and chemistry. The stiffness C_{12} of cubic diamond film consisting of fine grain of 10 - 60 nm was found to be quite large due to the graphite phase existing along the GB. A spherical indentation test assisted by highly sensitive microcrack detection method utilising acoustic emission (AE) and corrosion potential fluctuation (CPF) was developed for the fracture strength evaluation. AE and CPF were available for thick and thin film, respectively. The fracture strength, estimated from stress distribution calculation by finite element method (FEM), changed from 4.0 GPa to 6.4 GPa depending on film thickness and grain size.

Nowadays polycrystalline diamond film synthesised by chemical vapour deposition (CVDD) is an indispensable material in manufacturing tools such as machining tools, wear resistant parts, manufacturing dresser tools etc. For those applications, mechanical properties of CVDD are important factors that strongly affect their functions, and are remarkably changed by the microstructure of the film such as grain size, orientation and grain boundary (GB) structure. Therefore, it is necessary to evaluate mechanical properties of the CVDD. Conventional methods, however, are scarcely available for CVDD due to its high hardness of the diamond, high film stiffness, and being difficult to process. In this study, the authors developed advanced new methods which can evaluate mechanical properties (elastic stiffness and fracture strength) of polycrystalline diamonds and studied the relation between microstructure and the properties of the film.

Elastic stiffness was measured by the resonant-ultrasound spectroscopy coupled with laser Doppler interferometry (RUS/LDI). This system, developed by Ogi et al. [1-7], allows us to determine the stiffness coefficients: C_{ij} of the thin film by the inversion process. We measured the diagonal coefficients, C_{11} and C_{44} , and the off-diagonal coefficient C_{12} of the film, and discussed the relationship between the C_{12} and grain boundary chemistry based on the micromechanics model [8,9].

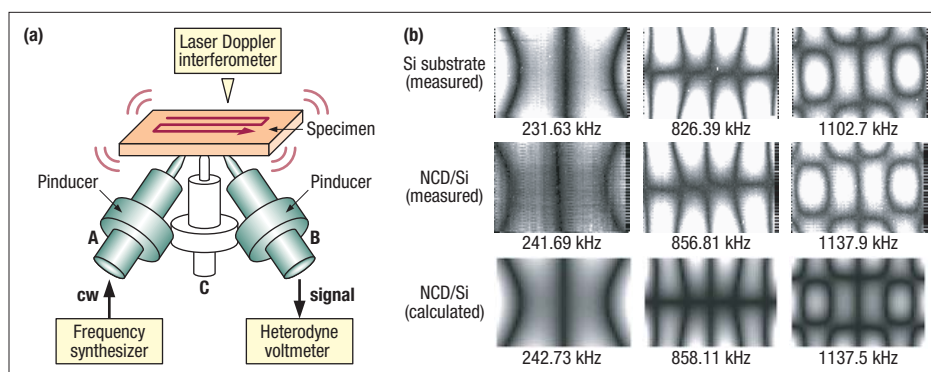
Fracture strength was measured by indentation test with spherical indenter. Kagawa et al. [10,11] developed a static fracture test of hard coatings by modifying the Hertzian fracture test [12]. In this test, detection of the first ring crack is of most importance and we developed a hybrid monitoring system using improved acoustic emission (AE) analysis method, classifying fracture mode and corrosion potential fluctuation (CPF).

Elastic stiffness evaluation

RUS/LDI method

Fig 1 (a) shows a setup of the RUS/LDI method. A rectangular-shaped specimen was held by three edge-shaped supports. Two supports with piezoelectric transducers of 10-MHz resonant frequency were utilised for vibration excitation and detection. The support A oscillates the specimen and the support B detects the resonance frequencies. By sweeping the frequency of the driving signal from 50 to 1500 kHz and acquiring the vibrational amplitude as a function of the frequency, we obtain a resonant spectrum.

Fig 1 Measurement setup of the RUS/Laser method (a) and distributions of out-of-plane vibration amplitude on resonating specimen (b)



As this method uses no coupling agent and apply no external force to the specimen, it can realise an ideal free vibration condition. We measured the resonance frequencies of the silicon substrate with and without the diamond film. Stiffness coefficients: C_{ij} were determined by the inverse processing of the frequency shift for each vibration mode of the specimens without and with the film. As the accurate mode identification is indispensable in this method, we measured profile of the out-of-plane displacement of the vibrating specimen at each resonance frequency using the laser-Doppler interferometer. Fig 1 (b) compares the measured and computed contour maps of out-of-plane displacement at three resonant frequencies. Here, the dark ridges designate the nodes of vibration. We observe excellent agreement between the contour maps of the specimen with the NCD film (the middle row) and computed one (the lowest row). We used resonance frequencies more than 25 for the determination of the two independent elastic constants of the diamond thin films.

Specimen

We prepared micrometer grain-size polycrystalline diamond (MCD) films and nanometer-size polycrystalline diamond (NCD) films by a hot filament CVD method using $CH_4/N_2/H_2$ gas mixture. The N_2 gas was used to enhance the renucleation rate and then to produce fine diamond grains of nanometer size. Surface SEM images of two CVD diamond film prepared are in Fig 2. Fig 2 (a) shows the surface of MCD film with well faceted diamond grains of 3-5 μm and (b) shows that of fine grained NCD film with grain size of 10 to 60 nm. We evaluated elastic stiffness of MCD and NCD films changing the film thickness deposited on monocrystal silicon of $6.0 \times 4.0 \times 0.4 \text{ mm}^3$.

Results and discussion

Fig 3 shows the thickness dependence of the three coefficients: C_{11} , C_{44} and C_{12} of the diamond film. The error bar was determined by taking both the contributions of the coefficients

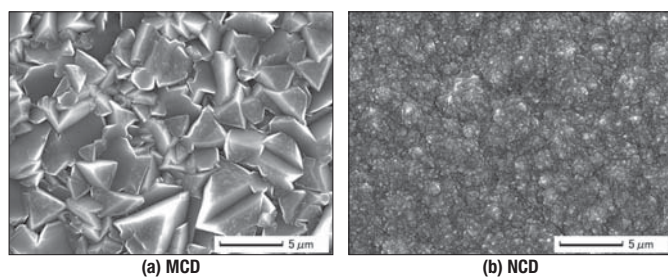


Fig 2 SEM images of CVD diamond films with different grain size

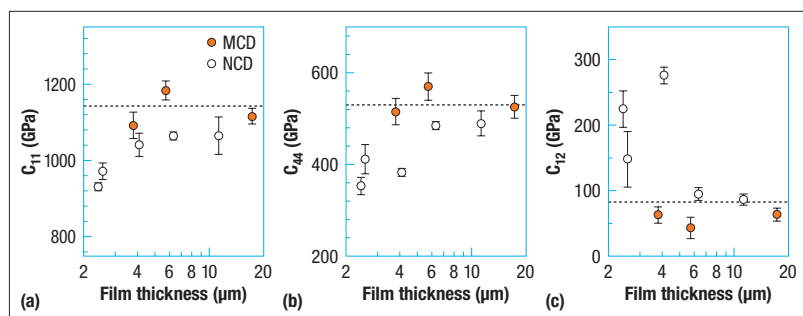


Fig 3 Stiffness coefficients as a function of thickness; (a), (b) the diagonal component and (c) the off-diagonal component

to the resonance frequencies and the distributions of the film thickness into account. Horizontal broken lines show the stiffness of an isotropic polycrystalline aggregates (says a bulk diamond). They are calculated by using the data of single-crystal diamond and the Hill-averaging method [13].

The following interesting facts are revealed.

- 1) For the MCD film thicker than 4 μm , both the diagonal (C_{11} , C_{44}) and off-diagonal coefficients (C_{12}) are close to those of the bulk diamond.
- 2) Stiffness coefficients of the NCD films are different from those of the MCD films. The diagonal components of the NCD films are smaller than those of the MCD films. The difference, however, tends to increase with a decrease of the film thickness.
- 3) The off-diagonal coefficient C_{12} of the thin NCD film ($< 4 \mu m$) is much larger than those of the bulk diamond and the MCD film.

These findings can be closely correlated with the structural configuration of the polycrystalline diamond, as discussed below.

We then attempted a micromechanics calculation for the models with randomly oriented thin pancake-shape inclusions at the grain boundaries (GBs). Two types of inclusion were considered. One is the microcrack and the other is the sp^2 -bonded graphite plates, whose c axes are normal to the grain boundaries. We calculated the elastic constants of two-phase composite with diamond grain and grain boundary (crack or graphite) utilising the Eshelby's equivalent inclusion theory [14] and Mori-Tanaka's mean field theory [15]. For the microcrack model, we set the moduli to be zero. For the pancake-shape graphite model, stiffness coefficients reported for a monocrystal graphite [16] ($C_{11}=1060$, $C_{33}=36.5$, $C_{12}=180$, $C_{13}=15$ and $C_{44}=0.3 \text{ GPa}$) are adopted. Results are shown in Fig 4. Three coefficients are calculated as a function of volume fraction of the inclusions. Aspect ratio of the inclusion was also changed from 100 to 1000.

For the microcrack model (Fig 4 (a)), both the diagonal and off-diagonal coefficients decreased with an increase of the volume fraction, indicating that the microcrack model explains the reduction of the diagonal coefficients but fails to explain the increase of the off-diagonal component. Contrary to this, graphite plate model (b) shows an increase of C_{12} and decrease of C_{11} and C_{44} with an increase of the volume fraction. This result strongly supports a concept that the large C_{12} of the NCD films is due to the thin graphitic phase along GBs.

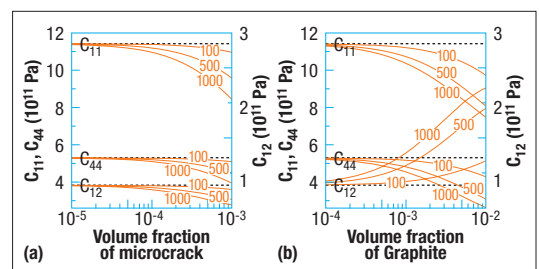


Fig 4 Micromechanics calculation of the elastic constants of polycrystalline diamond as a function of volume fraction of pancake-shape inclusion in the grain boundary changing aspect ratios of 100, 500 and 1000 in the cases of (a) microcrack and (b) graphite plate inclusion

Fracture strength evaluation

Spherical indentation test assisted by AE and CPF

We performed static indentation tests using natural diamond indenter with tip radius of $400\ \mu\text{m}$ to measure fracture strength of CVD diamond deposited on sintered silicon carbide (SiC) substrate. The indenter was indented onto polished diamond film by load controlling method. Loading rate was controlled at $0.08\ \text{N/s}$ or $0.2\ \text{N/s}$, and maximum force was sustained for 10 s. Here, the maximum force, F_{max} was changed between 10 to 196.2 N.

Fig 5 (a) shows an experimental setup of hybrid crack monitoring system of AE and CPF. Four small PZT-type AE sensors (PAC, Type PICO) were mounted on side surfaces of square specimen and monitored Lamb wave AEs during indentation test. Sensor outputs were amplified to 60 dB using pre-amplifiers (PAC), digitized by a fast A/D converter (Compu Scope, CS12100 Gage Applied Sciences Inc.) and fed to a personal computer. Sampling interval and points were set as 40 ns and 2048, respectively. We classified fracture modes or crack types by analysing the polarity distribution of the zeroth order symmetric mode (S_0 -mode) Lamb wave, according to the method proposed by Sato et al. [17]. This technique

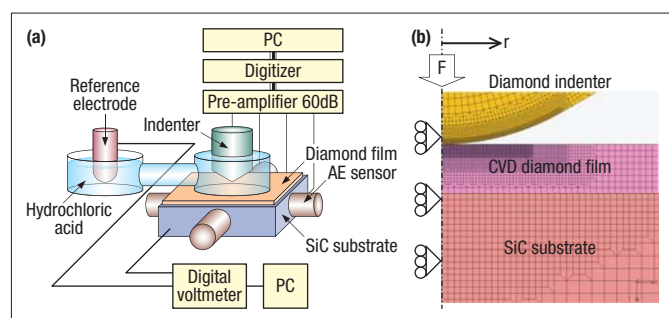


Fig 5 Experimental setup of hybrid indentation system of acoustic emission (AE) and corrosion potential fluctuation (CPF) (a) and the axial symmetric FEM model (b)

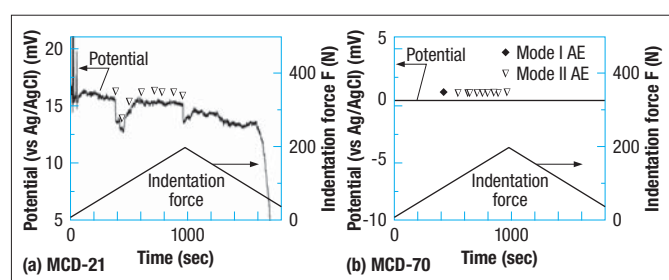


Fig 6 Potential curves with AE timings during indentation test for the MCD films

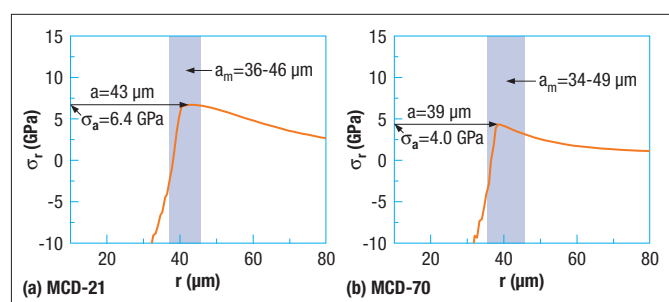


Fig 7 Surface stress distributions by FEM calculations

enables us to classify AEs into Mode-I and Mode-II fracture. The Mode-I crack produces S_0 -mode with a set of all (four) positive polarities. Mode-II crack produces S_0 -Lamb wave with mixed polarities of positive and negative.

Tests were performed in a solution to monitor the CPF which allows us to monitor the film damage sensitively. A 20 mm diameter plastic cell was glued on the specimen surface. This cell is connected to another cell with reference electrode of Ag/AgCl (GS-5015C: TOA-DKK). The solution was hydrochloric acid with a little additive (1 mol HCl + 0.01 mol KSCN). Output of the electrode was acquired by a digital volt meter (RE6871E: ADVANTEST) with the resolution of 1 mV at the time interval of 250 ms. When the solution penetrates into the sintered SiC substrate through the ring crack, we can detect a potential change to active direction by anodic dissolution of metallic elements along grain boundary of sintered SiC.

We evaluated the fracture strength of the diamond film from the largest tensile stress computed for the critical indentation load to produce the first Mode-I ring crack. The calculation was conducted for load control condition using a general purpose FEM program (MARC, K7-2). The axial symmetric model used for the simulation is shown in Fig 5 (b). Young's modulus and Poisson's ratio of the diamond films were measured by RUS/Laser method.

Two MCD films with different thicknesses of 21 and $70\ \mu\text{m}$ deposited on SiC substrate (6.0 mm thick) were prepared. Here we call those as MCD-21 and MCD-70 respectively. These films were polished by diamond grinding wheel to obtain clear observation of indented surface and to reduce friction between the indenter and diamond film.

Results and discussion

Fig 6 shows corrosion potential fluctuation and load history for the test of MCD-21 and MCD-70. AE generation timings were also plotted near the curve. Mode-I AE designated by ◆ corresponds to the ring crack generation while Mode-II (▽) AE the interfacial shear crack or slip noise between indenter and film surface. For the thin diamond film (MCD-21), the potential shifted to active side quickly at $F = 82\ \text{N}$ and recovered slowly after staying for about 50 seconds. Similar potential shift was also observed at $F = 194\ \text{N}$. We observed multiple ring cracks on the film surface after the test. Two potential shifts observed during loading correspond to the ring crack generations. The potential recovery is considered to be due to the crack closure by further indenting. The potential shifted to active side largely at $F = 75\ \text{N}$ during unloading. This occurred due to penetration of the solution into the ring crack again when the indenter departs from the film surface. No Mode-I AE or ring crack AE was detected for the test of thin MCD film. For thin film, released energy with crack generation is very small and AE is hardly detected, while the CPF can be easily detected because the crack opens quickly. Contrary to the thin diamond film, one Mode-I AE but no potential shift was detected for the thick diamond film (MCD-70). For thick film, the solution can not reach the substrate surface due to small opening of the crack. As the result, the corrosion potential does not show any shift. However AE was detected easily because large energy is released.

We next evaluated fracture strength of three diamond films utilising FEM. Ring cracks were detected at $F = 81.9\ \text{N}$ (MCD-21) and $F = 90.0\ \text{N}$ (MCD-70). Surface stress distributions at ring crack initiation were computed by FEM and shown in Fig 7.

Ring crack diameters (α_m), determined by a microscope, were shown with hatched bar in the figure. The radii (α) at the largest tensile stress (σ_a) agree well with the radii (α_m) of observed ring cracks. As a result, fracture strength of 6.4 and 4.0 GPa were obtained for MCD-21 and MCD-70 respectively.

The difference in strength between MCD-21 and MCD-70 originate in grain size of the film. MCD film grows columnar style along normal to the substrate surface indicating that the thicker film has larger grains at the surface than those near the interface. Fig 8 shows the surface SEM images of MCD-21 and MCD-70 as deposition condition (before polishing). MCD-21 consist of 3 ~ 7 μm -grains and MCD-70 of 10 ~ 18 μm -grains at the surface. The largest dormant defect most likely to causes fracture in brittle material. Size of defect depends on grain size of polycrystalline diamond film and crack propagates along the cleavage plane of (111) in diamond crystal. MCD-70 shows lower strength than MCD-21 due to large grain size.

Summary

Mechanical characteristics of polycrystalline CVD-diamond film were studied by developing new methods. Results are summarised below.

- 1) Resonant-ultrasound spectroscopy with the laser-Doppler interferometry determined the independent elastic constants of MCD and NCD films, and we found that both the diagonal and off-diagonal coefficients (C_{11} , C_{44}) are close to those of the bulk diamond for MCD film and NCD film poses quite large off-diagonal component (C_{12}) originating in graphite phase along grain boundary.
- 2) Fracture strength of MCD diamond films with different thicknesses were measured to be 4.0 to 6.4 GPa by spherical indentation test with AE and CPF, assisted with FEM analysis. The difference in strength could be explained considering the difference in grain size at the film surface generated by grain growth behaviour of CVD-diamond. We studied method to detect the first ring crack which is important for determination of the fracture strength. It was found that AE was available for thick film and CPF was available for thin film. ♦

Authors

R. Ikeda, Asahi Diamond Industrial Co Ltd, 787 Tabi, Ichihara, Chiba 290-0515, Japan.

H. Ogi, Osaka University, Toyonaka, Osaka 560-8531, Japan.

T. Ogawa and **M. Takemoto**, Aoyama Gakuin University, Sagamihara, Kanagawa 229-0885, Japan.

Acknowledgment

This research was conducted as part of the High-Technology Research Center Program and the Centre of Excellence (COE) Program, funded by the Ministry of Education, Cultures, Sports, Science and Technology of Japan.

This article is based on a paper presented at the 2nd International Industrial Diamond Conference held in Rome, Italy on April 19-20 2007 and is printed with kind permission of Diamond At Work Ltd.

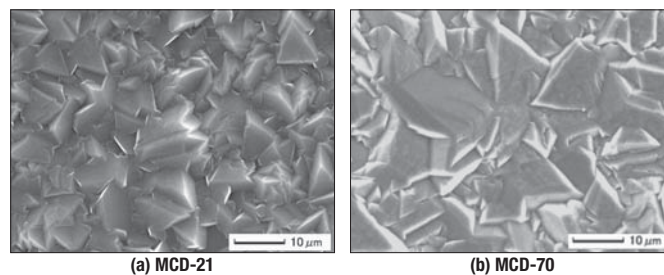


Fig 8 SEM images of CVD diamond films with different thickness

References

- [1] H. Ogi, G. Shimoike, M. Hirao, K. Takashima and Y. Higo, 'Anisotropic elastic-stiffness coefficients of an amorphous Ni-P film', *J. Appl. Phys.*, 91 [8] (2002) pp 4857-4862.
- [2] N. Nakamura, H. Ogi and M. Hirao, 'Elastic constants of chemical-vapour-deposition diamond thin films: resonance ultrasound spectroscopy with laser-Doppler interferometry', *Acta Mater.*, 52 [3] (2004) pp 765-771.
- [3] N. Nakamura, H. Ogi, T. Ono and M. Hirao, 'Determination of anisotropic elastic constants of superlattice thin films by resonant-ultrasound spectroscopy', *J. Appl. Phys.*, 97 (2005) p 013532.
- [4] N. Nakamura, H. Ogi, T. Ono, M. Hirao and M. Nishiyama, 'Elastic constants and magnetic anisotropy of Co/Pt superlattice: Resonance-ultrasound-spectroscopy method' *Jpn. J. Appl. Phys.* 44, 6B (2005) pp 4427-4430.
- [5] H. Ogi, K. Sato, T. Asada and M. Hirao, 'Complete mode identification for resonance ultrasound spectroscopy', *J. Acoust. Soc. Am.*, 112 [6] (2002) pp 2553-2557.
- [6] H. Ogi, H. Ledbetter, Y. Kawasahi and K. Sato, 'Acoustic spectroscopy of lithium niobate: Elastic and piezoelectric coefficients', *J. Appl. Phys.*, 92 [5] (1992) pp 2451-2456.
- [7] H. Ogi, M. Fukunaga, M. Hirao and H. Ledbetter, 'Elastic constants, internal friction, and piezoelectric coefficient of α -TeO₂', *Phys. Rev. B*, 69 (2004) p 024104.
- [8] H. Ogi, N. Nakamura, H. Tanei, M. Hirao, R. Ikeda and M. Takemoto, 'Off-diagonal elastic constant and sp²-bonded graphitic grain boundary in nanocrystalline-diamond thin films', *Appl. Phys. Lett.*, 86 (2005) p 231904.
- [9] R. Ikeda, H. Tanei, N. Nakamura, H. Ogi, M. Hirao, A. Sawabe and M. Takemoto, 'Elastic constant of nanocrystalline diamond film', *Diamond Relat. Mater.* (in press).
- [10] H. Kagawa, M. Ichikawa, T. Takamatsu and H. Kuwano, 'Evaluation of fracture strength of thin films by indentation with a small spherical indenter', *Trans. J. Soc. Mech. Eng. A60*, 570 (1994) pp 396-401.
- [11] H. Kagawa, M. Ichikawa, T. Takamatsu and H. Kuwano, 'Approximate expression for stress distribution in film subjected to indentation by spherical indenter', *Trans. J. Soc. Mech. Eng. A60*, 570 (1994) pp 416-420.
- [12] T. R. Wilshaw 'The Hertzian fracture test', *J. Phys. D: Appl. Phys.*, 4 (1971) pp 1567-1581.
- [13] O. L. Anderson, in *Physical Acoustics*, edited by W. P. Mason (Academic New York, 1965), Vol. IIIB, p 43.
- [14] J. D. Eshelby, 'The determination of the elastic field of an ellipsoidal inclusion, and related problems', *Proc. R. Soc. London, Ser. A* 241 (1957) pp 376-396.
- [15] T. Mori and K. Tanaka, 'Average stress in matrix and average elastic energy of materials with misfitting inclusions', *Acta Metall.*, 21 (1973) pp 571-574.
- [16] O. L. Blakslee, D. G. Proctor, E. J. Seldin, G. B. Spence and T. Weng, 'Elastic constants of compression-annealed pyrolytic graphite', *J. Appl. Phys.*, 41 [8] (1970) pp 3373-3382.
- [17] T. Sato, M. Takemoto and K. Ono, 'Effect of fracture dynamics in thin plate on the waveform and radiation pattern of the Lamb waves', *Jpn. J. Appl. Phys.*, 38, 5B (1999) pp 3139-3200.